ELSEVIER

Contents lists available at ScienceDirect

Journal of Magnetism and Magnetic Materials

journal homepage: www.elsevier.com/locate/jmmm





Crystallization and stability of rare earth iron garnet/Pt/gadolinium gallium garnet heterostructures on Si

Miela J. Gross ^a, Jackson J. Bauer ^b, Supriya Ghosh ^c, Subhajit Kundu ^c, Kensuke Hayashi ^b, Ethan R. Rosenberg ^b, K. Andre Mkhoyan ^c, Caroline A. Ross ^{b,*}

- ^a Department of Electrical Engineering and Computer Science, Massachusetts Institute of Technology, Cambridge, MA, USA
- b Department of Materials Science and Engineering, Massachusetts Institute of Technology, Cambridge, MA, USA
- ^c Department of Chemical Engineering and Materials Science, University of Minnesota, Minneapolis, MN, USA

ARTICLE INFO

Keywords: Rare earth iron garnets Magnetic insulators Spintronics Crystallization

ABSTRACT

The crystallization of rare earth iron garnet films such as dysprosium iron garnet on Si substrates provides a path for integration of these complex oxides into magnetic devices. We report the growth of 50–75 nm thick dysprosium yttrium iron garnet (YDyIG) films, deposited without a seed layer then crystallized by a 750 °C rapid thermal anneal, forming a polycrystalline film with grains of several μ m diameter containing radiating low-angle boundaries. The Y:Dy ratio affects the magnetization and anisotropy of YDyIG. Crystallization becomes more challenging as the garnet film thickness decreases. To crystallize thinner rare earth garnet films, tri-layer stacks consisting of a 50 nm thick gadolinium gallium garnet (GGG) seed layer, a 1.5 nm thick Pt diffusion barrier, and a 10 nm thick YDyIG film were prepared. The YDyIG/Pt/GGG tri-layers showed agglomeration of the Pt leading to a morphology consisting of a polycrystalline garnet film enriched with Dy and Fe and containing a layer of Pt nanoparticles embedded near its surface.

1. Introduction

Rare earth iron garnets ($RE_3Fe_5O_{12}$ or REIGs) are of great interest in the development of spintronic and magnonic devices due to their insulating ferrimagnetic characteristics [1–5]. Rare earth substitutions in the garnet structure enable fine tuning of the magnetic properties such as saturation magnetization, magnetic anisotropy, compensation temperature and Gilbert damping [6–8]. The low damping found in $Y_3Fe_5O_{12}$ (YIG) and Bi-substituted YIG and the moderate damping of $Tm_3Fe_5O_{12}$ lead to fast magnetization dynamics and domain wall motion [9–13]. Furthermore, perpendicular magnetic anisotropy (PMA) can be introduced into thin film REIGs via magnetoelastic anisotropy [14,15] or growth-induced anisotropy [16]. Thin films with PMA are advantageous for studying domain walls and chiral spin textures [17,18], which combined with their fast dynamics makes REIGs attractive for applications in domain wall-based spin logic and memory devices [19,20].

Incorporation of REIGs into devices requires the growth of thin film garnet films on silicon or other substrates. There have been several demonstrations of polycrystalline garnet growth on non-garnet substrates, in particular Bi, Ce and Tb iron garnets for magnetooptical applications [21,22] and Dy and Eu iron garnets with PMA [23], in which the garnets are typically grown by pulsed laser deposition at high substrate temperatures or by sputtering followed by annealing to crystallize the films [24,25]. Some compositions including YIG and TbIG crystallize without a seedlayer, but in other cases, notably Ce and Bicontaining garnets, a YIG seedlayer may be used to promote the formation of the garnet phase [21,26]. Bauer et al. [6] showed that films of Dy₃Fe₅O₁₂ (DyIG) can be crystallized on silicon without a seedlayer for thicknesses of 22 nm and above, but thinner films did not crystallize under the same annealing conditions. Another approach is to use remote epitaxy and transfer to produce single crystal garnet films, e.g. from a graphene-coated garnet substrate [27], but this process has been limited to films of order 100 nm thickness and above.

The importance of interfacial magnetic phenomena motivates the growth and characterization of sub-10 nm thick garnets on Si despite the difficulty in crystallizing such thin films. Aldosary et al. [28] showed epitaxial single crystalline YIG can be grown directly on 5 nm of Pt on a single crystal $Gd_3Ga_5O_{12}$ (GGG) substrate. This prompted our investigation of a tri-layer heterostructure of thin REIG/Pt/GGG/Si in which the GGG layer is intended to act as a virtual substrate, templating the

E-mail address: caross@mit.edu (C.A. Ross).

^{*} Corresponding author.

crystallization of the REIG, and the Pt acts as a diffusion barrier. GGG is used as a template layer instead of YIG because GGG is paramagnetic.

In this article we first describe the effects of Y substitution of Dy in reducing the anisotropy and lowering the magnetic moment of DyIG on silicon. We then report the thermal stability and microstructural development of heterostructures of 10 nm DyIG or Y-substituted DyIG $(Y_{1.5} \mathrm{Dy}_{1.5} \mathrm{Fe}_5 \mathrm{O}_{12}, \ \mathrm{YDyIG})/1.5$ nm of Pt/50 nm of GGG on Si. The Pt barrier was grown at room temperature to suppress dewetting observed at 400 °C and above [29], whereas the garnet layers were grown at a substrate temperature of 650 °C, and the tri-layer was finally crystallized by RTA at 750 °C for 5 min. We describe the evolution of the microstructure at different stages of the heterostructure growth, revealing interdiffusion between the garnet layers and thermal dewetting of the Pt layer, which led to a morphology of a polycrystalline garnet film containing a layer of subsurface Pt nanocrystals. This analysis of microstructural development provides insights into the stability of garnet/metal heterostructures.

2. Methods

52 nm DyIG and 75 nm YDyIG polycrystalline single-layer films on (100)-oriented Si with native oxide were grown via pulsed laser deposition (PLD) by alternating ablation of stochiometric DyIG and YIG targets. Y:Dy ratios in the codeposition were calculated based on the calibrated growth rate from each of the targets, which was 2 nm per 1000 laser shots. The 248 nm KrF laser had an energy of 350 mJ, a repetition rate of 10 Hz, and was focused to a fluence of 2 J/cm² at the target. The chamber was pumped to a base pressure of 5×10^{-6} Torr and an oxygen pressure of 150 mTorr was maintained during the deposition. The substrates were heated to 650 °C at a ramp rate of 20 °C/min prior to deposition and cooled at the same rate post-deposition. The films underwent an ex-situ rapid thermal anneal (RTA) at 750 °C for 5 min in oxygen using a MILA-5050 furnace.

The DyIG/Pt/GGG and YDyIG/Pt/GGG heterostructures on silicon were grown in one chamber without breaking vacuum. First, 50 nm of GGG was deposited via PLD using a stochiometric GGG target and the same deposition conditions as the DyIG and YDyIG films described above. After the chamber had cooled to $<60\,^{\circ}\mathrm{C}$ and pumped to $5\times10^{-6}\,\mathrm{Torr}$ base pressure, 1.5 nm of Pt was sputtered onto the samples in an argon pressure of 5 mTorr at 30 W from a Kurt J Lesker 5 cm diameter DC magnetron sputtering gun within the PLD chamber tilted 45° relative to the sample surface. Following sputtering, 10 nm of DyIG (or YDyIG) was deposited via PLD on the samples following the same process as for the single layer DyIG and YDyIG films described above. The samples were then removed from the chamber for an *ex-situ* RTA at 750 °C for 5 min.

Grazing incidence x-ray diffraction (GIXD) measurements were performed to analyze film crystallinity using a Rigaku Smartlab Multipurpose Diffractometer with a Cu Kα x-ray source. Film thickness for the 52 nm and 75 nm thick DyIG and YDyIG films was obtained using x-ray reflectivity measurements performed on a Bruker D8 High Resolution Diffractometer. Hysteresis curves of the films were measured using a Digital Measurements Systems Vibrating Sample Magnetometer Model 1660 with field applied both in plane (IP) and out of the plane (OP) of the substrate. Surface topography was investigated with a Bruker Icon Atomic Force Microscope (AFM) in the tapping mode using Bruker RTESP-300 tips. To observe grain structure, electron backscatter diffractometry (EBSD) was carried out on a Zeiss Merlin high resolution scanning electron microscope (SEM). EBSD images were taken with the sample holder tilted at 70° and the electron beam at an acceleration voltage of 15 kV and a working distance of 15 mm. The inverse pole figure (IPF) EBSD maps did not clearly resolve the grain shape, so image

quality (IQ) EBSD maps [30], in which the contrast is derived from the change in orientation between neighboring points on the sample were used to characterize the grain shape.

Scanning transmission electron microscopy (STEM) imaging and energy dispersive X-ray (EDX) spectroscopy were used to characterize the structure and chemical composition of the heterostructures. Cross-sectional samples of the heterostructures were prepared using a focused ion beam (FIB) on a dual-beam FEI Helios Nanolab G4 FIB-SEM system. A 30 keV Ga ion beam was used to thin down the TEM lamella and finally a 2 keV ion-beam was used to remove damaged surface layers. The samples were coated with an amorphous carbon layer prior to the sectioning to prevent damage to the surface on ion-beam exposure.

High angle annular dark-field (HAADF)-STEM imaging and STEM-EDX elemental mapping were performed on an aberration-corrected FEI Titan G2 60–300 (S)TEM equipped with a monochromator, CEOS DCOR probe corrector and Super-X EDX spectrometer. The microscope was operated at 200 keV with a probe current of 80 pA. The HAADF images were collected with a probe convergence angle of 25.5 mrad and detector inner and outer collection angles of 55 and 200 mrad respectively.

3. Results

We first describe the microstructure and properties of single layer 52 nm thick DyIG and 75 nm thick YDyIG films grown directly on (100)-oriented silicon then annealed. Grazing incidence X-ray diffraction (GIXD) of the 52 nm DyIG/Si film is shown in Fig. 1a. All peaks can be indexed to a polycrystalline garnet phase without detectable secondary phases. An AFM scan, Fig. 1b, shows grains roughly 3 μm in diameter, consistent with our earlier work on similar films [6]. Prior work indicated that DyIG films prepared under these conditions had a Dy:Fe ratio that matched the target composition [8]. Like the DyIG, the YDyIG films also exhibit only garnet peaks and grains of a few μm in diameter once annealed.

Hysteresis loops for 52 nm DyIG on Si, Fig. 1c, show an out of plane easy axis with high remanence, a saturation magnetization (Ms) of 30 kA m⁻¹, and coercivity $\mu_0 H_C = 300$ mT. The in-plane (IP) hysteresis loop is characteristic of a hard-axis with an anisotropy field of $\mu_0 H_K = 750$ mT. The film therefore exhibits PMA. There is zero net magnetocrystalline anisotropy because the grains in the polycrystalline films have random orientations, and growth induced anisotropy is not expected to contribute to the net anisotropy since the films are crystallized by post-growth annealing which eliminates any preferential site ordering. The PMA is therefore attributed to thermal mismatch strain between the garnet film and Si substrate, as discussed previously [6]. On cooling from the annealing temperature, the DyIG thermal contraction is greater than that of Si [31,32], leaving the DyIG in IP tension. Both magnetostriction coefficients λ_{100} and λ_{111} of bulk DyIG are negative leading to a negative magnetostriction coefficient for polycrystalline DyIG of $\lambda_s = -8.54 \times 10^{-6}$ [33]. From the analysis in [6] and the temperature-dependent (isotropic) thermal expansion coefficients of the silicon substrate [32] and the garnet [34,35] a magnetoelastic anisotropy of 12.9 kJ $\,\mathrm{m}^{-3}$ is expected on cooling. The magnetoelastic anisotropy is sufficient to overcome the shape anisotropy ($\mu_0 M_s^2/2$ [36]) of 565 J m⁻³ yielding a film with PMA. An estimate of anisotropy field $H_K=2K/\mu_0M_s$ where K is the total anisotropy gives $\mu_0H_K=820$ mT, in reasonable agreement with the anisotropy field of 750 mT measured from the hard axis loop.

To modify the anisotropy, coercivity, and magnetization of the DyIG films on Si, Y was substituted for Dy to yield $Y_xDy_{3-x}Fe_5O_{12}$. Substitution of Y lowers the dodecahedral sublattice moment, hence lowering the

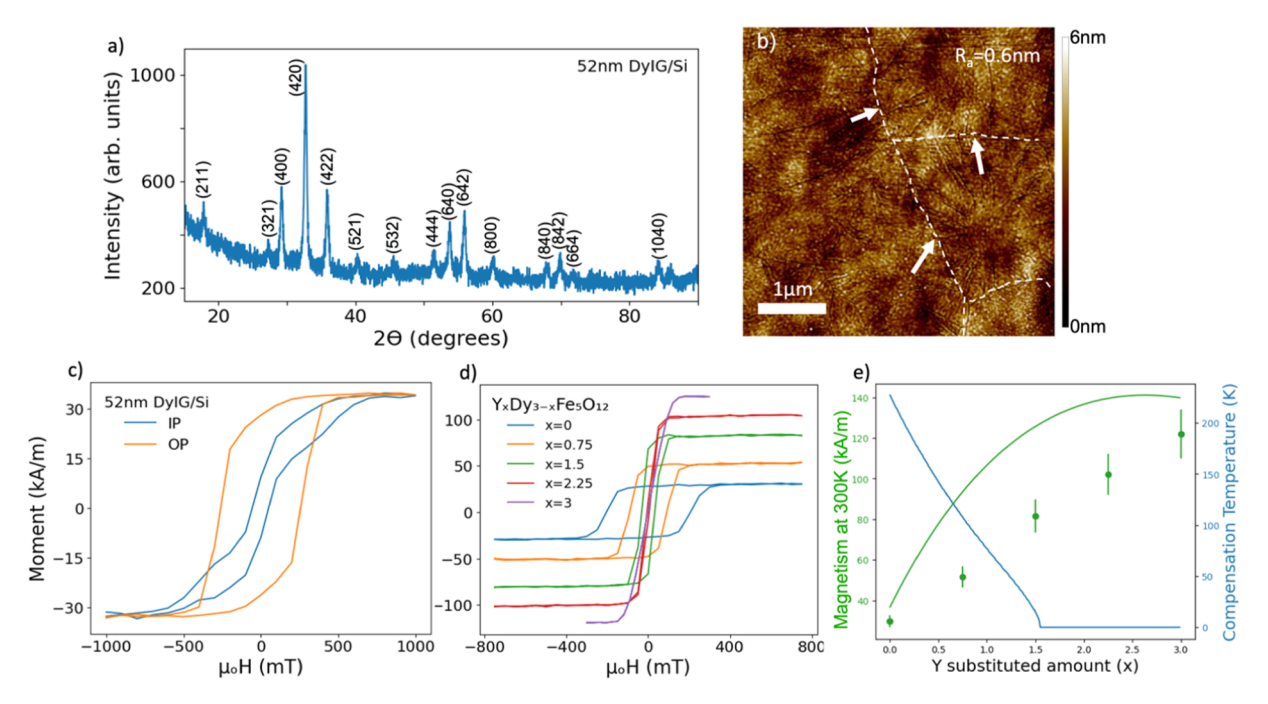


Fig. 1. Characterization of 52 nm DyIG/Si and 75 nm thick YDyIG/Si. a) GIXD scan of DyIG/Si shows peaks corresponding to single phase polycrystalline garnet. b) 5 μ m by 5 μ m AFM image of DyIG/Si surface that shows grains roughly 3 μ m in size. A few of the grain boundaries are indicated with dashed lines and arrows on the right side of the image. The film has an average roughness of 0.6 nm. c) Hysteresis loops for IP and OP applied field for DyIG/Si, showing PMA. d) Hysteresis loops measured in the OP direction of YDyIG with composition $Y_xDy_{3-x}Fe_5O_{12}$. e) Saturation magnetization at 300 K and compensation temperature as a function of Y content in $Y_xDy_{3-x}Fe_5O_{12}$ from MFC model. Points represent experimental data from d).

compensation temperature ($T_{comp}=220~K$ for bulk DyIG [37,38]) and raising the room temperature M_s . Y substitution also lowers the magnetostriction coefficient and hence the magnetoelastic anisotropy [33]. The increasing M_s from 30 to 140 kA m⁻¹ and the decreasing magnetostriction lead to a transition from PMA to an in-plane easy axis as the Y content increases. The coercivity μ_0H_C also decreases from 250 mT to < 1~mT for the OP loops as the Y fraction increases.

Dionne et al. [39] developed a molecular field coefficient (MFC) model to calculate the magnetic moment versus temperature of REIGs with various cation site occupancies. This model was used to calculate the M_s of $Y_xDy_{3-x}Fe_5O_{12}$ along with the compensation temperature as a function of Y substitution, Fig. 1e. This prediction is compared with experimental results from the room temperature out of plane (OP) hysteresis curves of 75 nm thick $Y_xDy_{3-x}Fe_5O_{12}$ films with five different Y:Dy ratios (Fig. 1d). The experimental room temperature M_s values follow the trend of the MFC model but are consistently lower in magnitude which may indicate incomplete crystallization of the film.

The foregoing results show that for this film thickness range (52-75 nm) and annealing conditions ($750\,^{\circ}$ C, $5\,$ min), DyIG and YDyIG crystallize as a single-phase garnet on Si without requiring a seed layer.

However, earlier work [6] showed that DyIG films below 22 nm thickness grown on Si did not crystallize under the same annealing conditions. To promote the crystallization of thinner magnetic garnet films on Si, we therefore investigate the use of a seed layer of paramagnetic GGG. REIG/GGG heterostructures were prepared and annealed (Fig. S1 in the Supplementary Information) but showed considerable diffusion of the RE and Fe into the GGG layer, especially evident at the grain boundaries of the seedlayer if the GGG is annealed before the REIG is deposited. Dilution of the Fe lowers the Curie temperature of the garnet and reduces its room temperature magnetic moment. This undesirable interdiffusion between the garnet layers suggests the necessity of a diffusion barrier layer between the REIG and the GGG seed layer. Aldosary et. al. [28] introduced 5 nm of Pt between a (110)-oriented garnet substrate and 30-80 nm YIG film which led to epitaxial single crystalline growth of the YIG. In this work, we selected 1.5 nm Pt thickness because 2-5 nm thick films of sputtered Pt on a crystallized GGG layer exhibited increasing roughness, whereas 1 nm Pt was discontinuous.

Heterostructures of 10 nm DyIG/1.5 nm Pt/50 nm GGG and YDyIG $(Y_{1.5}Dy_{1.5}Fe_5O_{12})/Pt/GGG$ were prepared in a multi-step process as shown in Fig. 2. Fig. 3a highlights the crystallinity of the 10 nm DyIG/

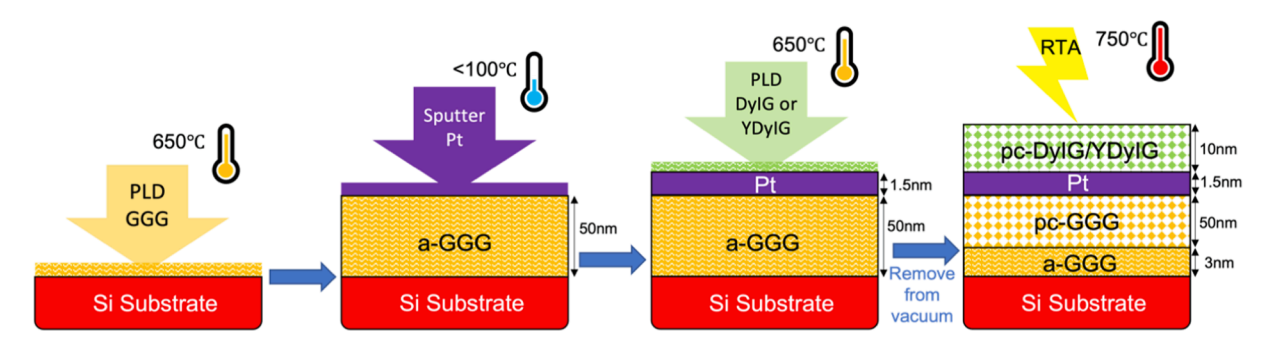


Fig. 2. Heterostructure growth process of DyIG/Pt/GGG/Si and YDyIG/Pt/GGG/Si. Amorphous and polycrystalline phases of the garnets are labeled as a and pc respectively. The GGG seedlayer is deposited, cooled before Pt growth, then heated for REIG growth and the resulting trilayer is then annealed.

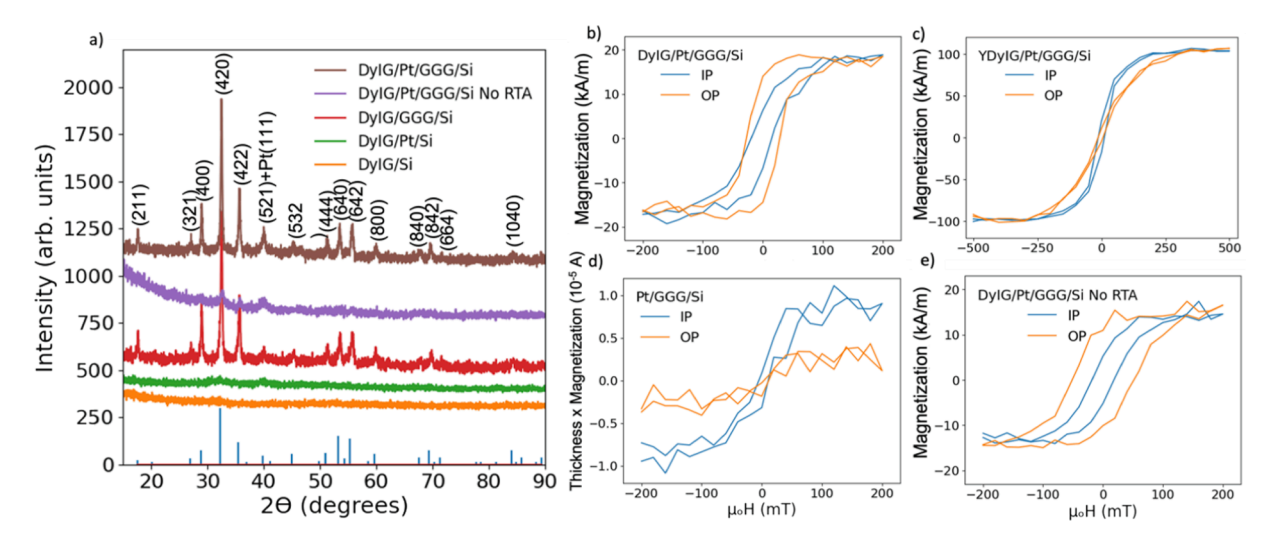


Fig. 3. a) GIXD of the DyIG/Pt/GGG/Si heterostructure and partial film stacks after RTA unless otherwise indicated. Data has been vertically shifted for clarity and the diffraction peaks and intensities of garnet are marked on the horizontal axis with blue bars of height proportional to the intensity of the powder diffraction peaks. b-e) VSM hysteresis loops measured in IP and OP field directions of b) DyIG/Pt/GGG/Si after annealing, c) YDyIG/Pt/GGG/Si after annealing, d) Pt/GGG/Si reference normalized by area, and e) DyIG/Pt/GGG/Si without RTA. The sample of d) has a magnetic moment over an order of magnitude smaller than the samples with the DyIG/YDyIG layer.

1.5 nm Pt/50 nm GGG stack before and after annealing, as well as control stacks of 10 nm DyIG/50 nm GGG, 10 nm DyIG/1.5 nm Pt and 10 nm DyIG, assessed using GIXD. Without the GGG templating layer, no garnet peaks are visible from the DyIG layer grown directly on Si or on Pt/Si. In contrast, when the GGG templating layer is present, garnet peaks are observed, though it is not possible to distinguish whether they originate from GGG, from DyIG, or from an interdiffused garnet layer due to the close lattice match.

The DyIG/GGG film showed no magnetic hysteresis, attributed to interdiffusion of the Fe and Dy into the GGG during annealing leading to a paramagnetic garnet. In contrast, annealed DyIG/Pt/GGG/Si and YDyIG/Pt/GGG/Si did show magnetic hysteresis, Fig. 3b,c. The OP loop of the DyIG/Pt/GGG/Si shown in Fig. 3b has a magnetization of $M_s=17~\rm kA/m$ and a coercivity of $\mu_0H_C=40~mT.$ In contrast, YDyIG/Pt/GGG/Si showed a coercivity μ_0H_C less than 1 mT, an IP easy axis (Fig. 3c), and an M_s of 100 kA/m. In both samples the magnetic characteristics appear consistent with the presence of a 10 nm thick DyIG or YDyIG layer

respectively, with magnetization in the range of the values of Fig. 1c, d and bulk material [40] considering the uncertainties in film thickness and accuracy of the VSM measurements. However, further magnetic and microstructural analysis paints a more complex picture of the annealed tri-layer garnet/Pt/garnet heterostructure.

To identify the origin of the magnetic signal, several partial film stacks were compared. Fig. 3d shows VSM hysteresis loops of a sample of Pt/GGG/Si measured after 750 °C RTA. The effective magnetic signal (moment divided by the nominal volume of the DyIG film) is over an order of magnitude smaller than that of the DyIG/Pt/GGG/Si and YDyIG/Pt/GGG/Si films, indicating that the magnetism of the tri-layer heterostructure comes from the magnetic garnet layer and not from other layers or from the substrate. Fig. 3e shows VSM of a DyIG/Pt/GGG/Si sample before RTA. The M_s of the unannealed film is similar to that of the annealed film but the loops indicate lower anisotropy. These results show that the DyIG contributes a magnetic signal even prior to RTA which may originate from partial crystallization during its growth

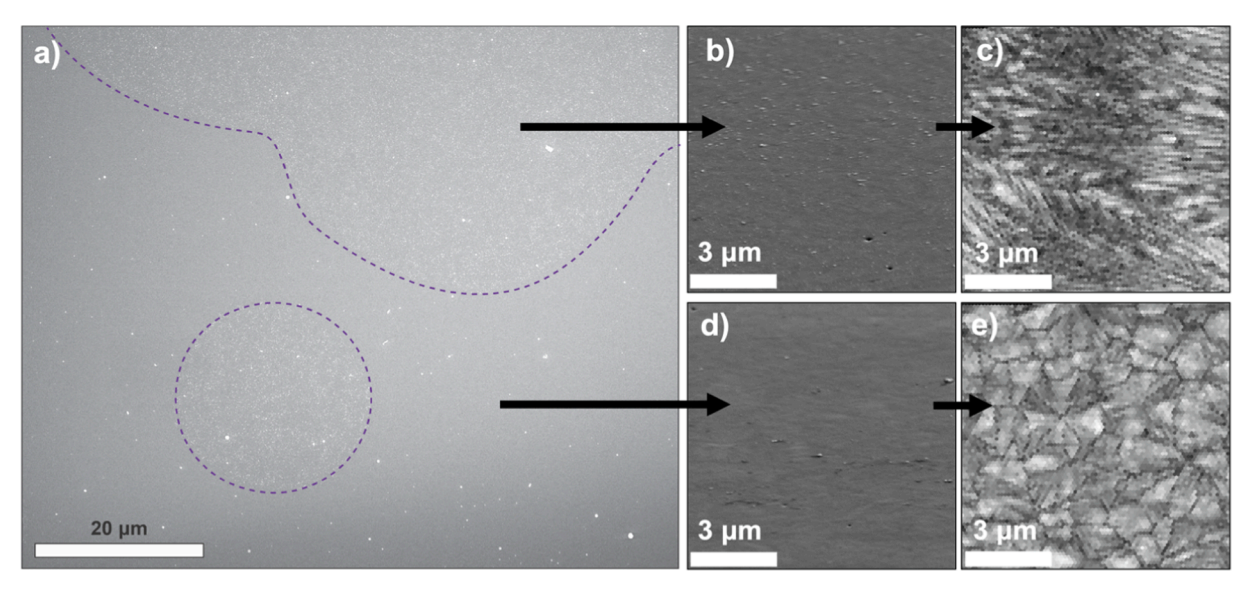


Fig. 4. a) Top surface SEM top surface image of DyIG(10 nm)/Pt(1.5 nm)/GGG(50 nm)/Si heterostructure. b) Zoomed SEM image and c) image quality EBSD of circular region showing common orientation over $10 \mu m$ area. d) Zoomed SEM image and e) image quality EBSD of area outside large circular region showing $1-3 \mu m$ grains of garnet. b) and c) shows a large grain with radiating contrast and d) and e) shows equiaxed grains.

at 650 °C on the Pt/GGG. The GIXD, Fig. 3a, indicates a weak garnet peak as well as a Pt peak prior to RTA which supports the hypothesis of partial crystallization of the DyIG or GGG during growth.

The microstructure of the tri-layer films after annealing at 750 °C was characterized using a combination of SEM, EBSD and HAADF-STEM imaging with spatial EDX maps. The top-view SEM images from the DyIG/Pt/GGG/Si stack (Fig. 4a) show large circular regions about 50 μm in size which appear to have Pt nanocrystals embedded on the top surface, surrounded by smoother regions with finer-scale features. Zoomed top surface SEM images of both areas are shown in Fig. 4b,d. To understand the garnet grain orientation in these regions, EBSD maps were obtained, Fig. 4c,e. In general, inverse pole figure (IPF) EBSD maps are used to quantify grain orientation to resolve the microstructure. When grains are inhomogeneous or strained, however, the intensity and sharpness of the electron diffraction spots are reduced and the IPF EBSD maps may not clearly resolve the grain shape. This was the case here, and therefore image quality (IQ) EBSD maps [30], in which contrast is derived from diffraction intensity and sharpness, were used to characterize the grain shape. The IQ-EBSD map highlights grain boundaries and the grain structure rather than grain orientation. IQ-EBSD of the outer smoother region, Fig. 4e, shows garnet grains roughly 1–3 µm in diameter, each with a radiating pattern of lines resembling that seen in the top surface of grains of YIG and DyIG films [6,12]. The line patterns are believed to originate from instability of the growth front as the grains grow into the amorphous region, but the crystal orientation on either side of the radiating lines is almost identical. The straight grain boundaries indicate that the grains nucleated simultaneously and grew to impingement. Fig. 4c shows IQ-EBSD maps from the circular granular region. The region shares a common orientation despite the presence of the radiating lines, indicating it is a large garnet grain. We hypothesize that the large grain is formed by secondary grain growth during the final 750 $^{\circ}\text{C}$ RTA step.

HAADF-STEM cross-sectional imaging of both DyIG/Pt/GGG and YDyIG/Pt/GGG shows that the garnet layers are polycrystalline with nanoparticles embedded near the top surface (Fig. 5). The YDyIG/Pt/GGG shows multiple vertical grain boundaries, Fig. 5a and Figure S2. The GGG lattice disappears within the bottom 3 nm of the layer, indicating an amorphous layer (see Fig. 5a). Compositional line scans suggest that the Gd:Ga ratio is higher in the amorphous layer at the bottom of the GGG film, which may be a result of rejection of excess Gd during crystallization (see Fig. S3b and Fig. S4b).

Most of the vertical grain boundaries are low angle, according to Fast Fourier Transforms (FFTs) of the atomic resolution HAADF images, Figure S2. This is in good agreement with the EBSD orientation maps shown in Fig. 4, where radiating line patterns are visible within individual grains. A few of the grain boundaries are high angle and spaced on the order of μ m apart. This is consistent with the model that the garnet film consists of 1–3 μ m grains but within the grains, radiating linear features correspond to low angle grain boundaries. STEM-EDX elemental maps show that the nanocrystals of about 13 nm diameter at the top surface are predominantly Pt, indicating that dewetting occurs during the synthesis of the heterostructure. No distinct YDyIG layer was observed near the top surface, and the Fe, Dy, and Y signals were difficult to detect. This is attributed to diffusion of the Fe and Dy ions into the GGG layer during growth and/or annealing (see Fig. S3).

The DyIG/Pt/GGG/Si heterostructure showed a similar morphology of Pt nanocrystals atop a 50 nm crystalline garnet film and again 3 nm of amorphous material at the GGG/Si interface. STEM-EDX elemental maps show that the top ~ 10 nm of the garnet layer is rich in Dy and Fe (Fig. 5c). SEM images also show the presence of Pt nanocrystals about

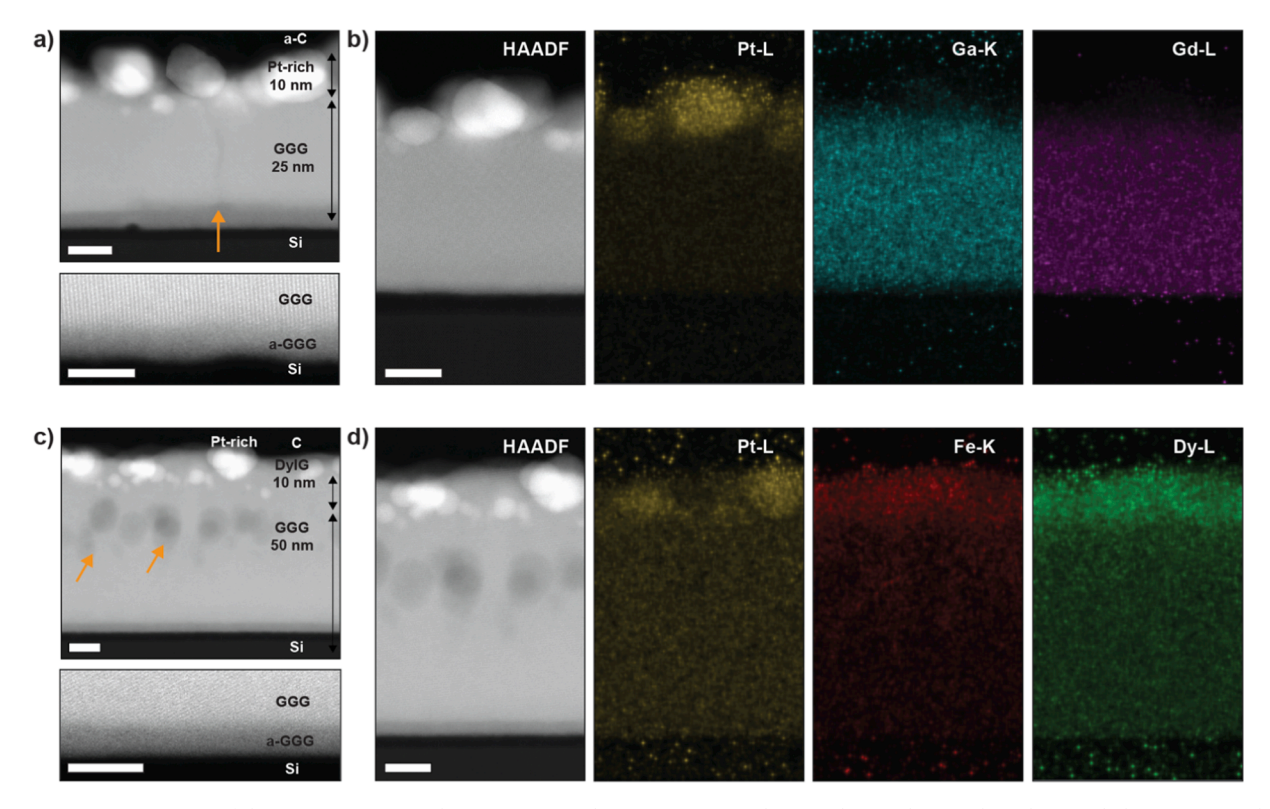


Fig. 5. a) HAADF-STEM image of the YDyIG/Pt/GGG/Si heterostructure. The orange arrow indicates a low-angle grain boundary. Scale bar is 10 nm. The lower panel is a high magnification section of the GGG-Si interface showing an intermediate amorphous GGG (a-GGG) layer between the crystalline GGG and Si/SiO₂ substrate. Scale bar is 5 nm. b) STEM-EDX compositional maps for the Pt, Ga, and Gd. Scale bar is 10 nm. EDX composition maps and concentration profiles across the heterostructure are shown in Fig. S3. c) HAADF-STEM image of the DyIG/Pt/GGG/Si heterostructure. Regions of darker contrast within the GGG layer are indicated by arrows where Fe and Dy are at higher concentrations. Scale bar is 10 nm. Panel at bottom shows high magnification section of the GGG-Si interface. Scale bar is 5 nm. d) STEM-EDX compositional maps (in at%) for Pt, Fe, and Dy. A DyIG-rich layer is present. Scale bar is 10 nm. Elemental distributions and concentration profiles across the heterostructure are shown in Fig. S4.

25 nm in size on the top surface (Fig. 4a). In addition, some regions of darker contrast are visible in the HAADF-STEM images of the GGG garnet layer (Fig. 5c,d), which correspond to higher concentrations of Fe and Dy as seen in the STEM-EDX maps (also see Fig. S4).

From the STEM analysis, it is evident in both samples the Pt layer undergoes a dewetting process either during the high temperature growth of the top DyIG garnet at 650 °C or during the RTA at 750 °C, causing the Pt to migrate to the top surface [29]. By comparing the GIXD scans of DyIG/Pt/GGG/Si film before and after RTA (Fig. 3a), the Pt (111) peak becomes more intense and narrower after RTA, suggesting that agglomeration of the Pt occurred during RTA despite DyIG encapsulating the Pt layer. To investigate the effects of the top garnet layer on the dewetting of Pt, 42 nm of YDyIG was grown on top of 1.5 nm of Pt on silicon and then annealed at 750 °C for 5 min. An SEM image of the top surface (Fig. S5) shows large particles of bright contrast. This indicates that dewetting occurs despite the 42 nm thick oxide layer covering the Pt, i.e. an encapsulating garnet layer over the Pt did not prevent agglomeration during annealing.

To further clarify the microstructural evolution of the Pt, AFM images were taken at several stages of processing of DyIG/Pt/GGG/Si stacks (Fig. 6). The surface of 50 nm thick GGG grown at 650 °C on Si before and after RTA at 750 °C for 5 min is shown in Fig. 6a,b respectively. The roughness (Ra) decreased from 1.1 nm as grown to 0.3 nm after RTA, indicating that the GGG becomes smoother as it crystallizes. During growth of the tri-layer stack, Pt is deposited on unannealed GGG and the initial roughness, which is on the order of the Pt thickness, is expected to lead to a discontinuous Pt film. This Pt readily dewets on subsequent heating, since dewetting is promoted by thickness fluctuations or porosity [29]. Fig. 6c shows 60 °C-deposited Pt/650 °C-deposited GGG/Si which has a surface roughness of 0.8 nm indicating that the as-grown Pt does not increase the roughness of the as-grown GGG. After RTA of the uncapped Pt/GGG/Si film, the Pt has dewetted into 50 – 100 nm-diameter islands as seen in Fig. 6d. Fig. 6e,f show images of the tri-

layer heterostructure DyIG/Pt/GGG/Si before and after RTA, where surface roughness is seen to increase after annealing.

The foregoing results show that the discontinuous thin Pt on the asgrown GGG layer is vulnerable to dewetting, which occurs primarily during the RTA of the full stack after the top layer of DyIG has been grown at 650 °C. Without the DyIG top layer, RTA generates large Pt particles (up to 100 nm) indicating a high Pt mobility at 750 °C. When the same process is applied to the tri-layer, the DyIG top layer suppresses but does not prevent the agglomeration of the Pt, and smaller particles are formed. Once the Pt is discontinuous it no longer serves as an effective barrier and the garnet layers interdiffuse during RTA. The secondary grain growth in the garnet is associated with a coarsening of the Pt nanoparticles above the recrystallized regions. The requirement of a 750 °C RTA to crystallize the as-grown garnet is therefore too high to maintain the integrity of the Pt layer, and its role as a diffusion barrier is compromised. Reducing the crystallization temperature of the garnet, smoothing the GGG seed layer surface, and using a more refractory material as diffusion barrier might allow the stack to be formed and crystallized without degrading the topography.

4. Conclusion

We have examined the crystallization of DyIG and YDyIG films directly on a Si substrate using a rapid thermal anneal. Films of DyIG with thickness 52–75 nm crystallized as single-phase garnet on Si after RTA at 750 $^{\circ}\text{C}$ to form grains with diameters of several μm exhibiting radiating patterns consisting of low angle grain boundaries. The out of plane easy axis is a result of tensile strain in the DyIG film due to thermal expansion mismatch, with crystallization-induced densification likely also contributing to the tensile strain. Substitution of Y for Dy yields a series of films with decreasing coercivity and PMA along with increasing magnetic moment at room temperature as expected from molecular field coefficient modeling. This allows the anisotropy and magnetic moment

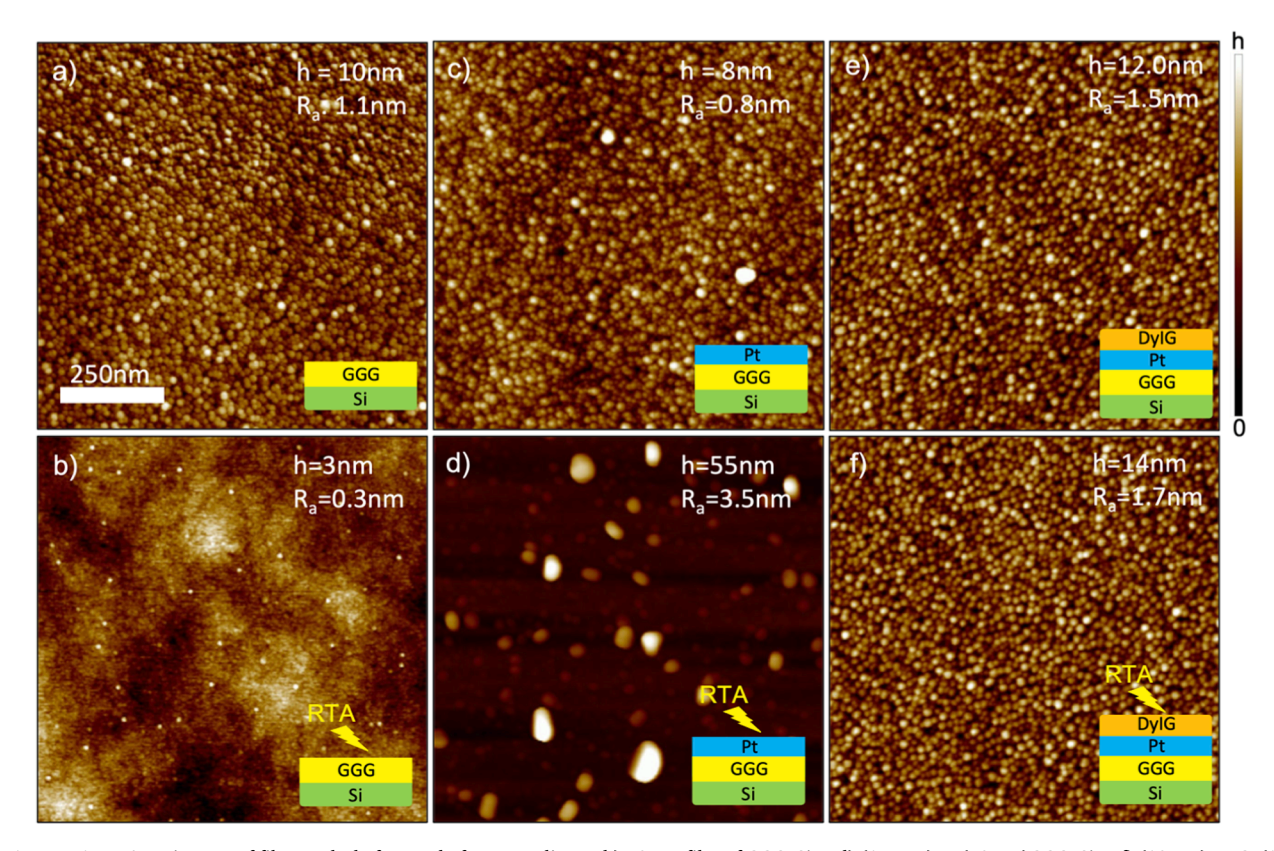


Fig. 6. 1 μ m \times 1 μ m AFM images of film stacks before and after annealing. a-b) 50 nm film of GGG/Si. c-d) (1.5 nm)Pt/(50 nm)GGG/Si. e-f) (10 nm)DyIG/(1.5 nm) Pt/(50 nm)GGG/Si. a), c), and e) are as-grown and b), d), and f) are annealed at 750 °C for 5 min. h represents the vertical height range on the color scale bar.

of YDyIG films to be tuned over a wide range via composition control.

However, as the film thickness decreases, crystallization of the films into single-phase garnet is impeded. This prompts the inclusion of a templating layer of paramagnetic GGG separated by a Pt diffusion barrier. Attempts to form 10 nm thick DyIG and YDyIG on Si by using a GGG seed layer/Pt diffusion barrier led to dewetting of the embedded Pt layer to form metallic nanoparticles during RTA. Interdiffusion of the DyIG and GGG then yields a diffuse interface. Although the magnetic moment of the DyIG/Pt/GGG and YDyIG/Pt/GGG are consistent with the nominally 10 nm thick DyIG and YDyIG layers, the presence of embedded Pt particles and the diffuse interface led to a low crystal quality of the thin iron garnet. These results give insights into garnetmetal heterostructure growth and microstructural evolution that are relevant for fabrication and applications of garnet-metal stacks.

CRediT authorship contribution statement

Miela J. Gross: Methodology, Investigation, Formal analysis, Software, Validation, Writing – original draft, Visualization. Jackson J. Bauer: Conceptualization, Investigation, Software. Supriya Ghosh: Investigation, Formal analysis, Visualization. Subhajit Kundu: Investigation. Kensuke Hayashi: Investigation, Formal analysis, Visualization. Ethan R. Rosenberg: Investigation. K. Andre Mkhoyan: Writing – review & editing. Caroline A. Ross: Writing – review & editing, Supervision.

Declaration of Competing Interest

The authors declare that they have no known competing financial interests or personal relationships that could have appeared to influence the work reported in this paper.

Acknowledgements

The authors acknowledge support of SMART, one of seven centers of nCORE, a Semiconductor Research Corporation program, sponsored by the National Institute of Standards and Technology (NIST). Part of this work was carried out in the shared experimental facilities of MIT's Center for Materials Science and Engineering, NSF DMR 1419807. JJB acknowledges support of NSF DMR 1808190. Parts of this work were carried out in the Characterization Facility, University of Minnesota, which receives partial support from the NSF through the MRSEC (DMR-2011401) and the NNCI (EECS-2025124) programs.

Appendix A. Supplementary data

Supplementary data to this article can be found online at https://doi.org/10.1016/j.jmmm.2022.170043.

References

- [1] Y. Kajiwara, et al., Transmission of electrical signals by spin-wave interconversion in a magnetic insulator, Nature 464 (7286) (2010) 262–266, https://doi.org/ 10.1038/nature08876.
- [2] C.O. Avci, et al., Current-induced switching in a magnetic insulator, Nat. Mater. 16 (3) (2017) 309–314, https://doi.org/10.1038/nmat4812.
- [3] M. Montazeri, et al., Magneto-optical investigation of spin-orbit torques in metallic and insulating magnetic heterostructures, Nat. Commun. 6 (2015) 1–9, https://doi. org/10.1038/ncomms9958.
- [4] J. Chen, et al., Strong Interlayer Magnon-Magnon Coupling in Magnetic Metal-Insulator Hybrid Nanostructures, Phys. Rev. Lett. 120 (21) (2018) 2–7, https://doi. org/10.1103/PhysRevLett.120.217202.
- [5] L.J. Cornelissen, J. Liu, R.A. Duine, J. Ben Youssef, B.J. Van Wees, Long-distance transport of magnon spin information in a magnetic insulator at room temperature, Nat. Phys. 11 (12) (2015) 1022–1026, https://doi.org/10.1038/nphys3465.
- [6] J.J. Bauer, et al., Dysprosium Iron Garnet Thin Films with Perpendicular Magnetic Anisotropy on Silicon, Adv. Electron. Mater. 6 (1) (2020) 1900820, https://doi. org/10.1002/aelm.201900820.

- [7] O. Ciubotariu, A. Semisalova, K. Lenz, M. Albrecht, Strain-induced perpendicular magnetic anisotropy and Gilbert damping of Tm3Fe5O12 thin films, Sci. Rep. 9 (17474) (2019), https://doi.org/10.1038/s41598-019-53255-6.
- [8] J.J. Bauer, et al., Magnetic proximity effect in magnetic-insulator/heavy-metal heterostructures across the compensation temperature, Phys. Rev. B 104(094403) (2021), doi: 10.1103/PhysRevB.104.094403.
- [9] H. Chang, et al., Nanometer-Thick Yttrium Iron Garnet Films with Extremely Low Damping, IEEE Magn. Lett. 5 (2014) 1–4, https://doi.org/10.1109/ LMAG.2014.2350958.
- [10] C. Hauser, et al., Yttrium Iron Garnet Thin Films with Very Low Damping Obtained by Recrystallization of Amorphous Material, Sci. Rep. 6 (2016), https://doi.org/ 10.1038/srep20827.
- [11] L. Caretta, et al., Relativistic kinematics of a magnetic soliton, Science 370(6523) (1979) 1438–1442, 2020, doi: 10.1126/science.aba5555.
- [12] T. Fakhrul, S. Tazlaru, L. Beran, Y. Zhang, M. Veis, C.A. Ross, Magneto-Optical Bi: YIG Films with High Figure of Merit for Nonreciprocal Photonics, Adv. Opt. Mater. 7 (13) (2019) 1–9, https://doi.org/10.1002/adom.201900056.
- [13] C.O. Avci, A. Quindeau, M. Mann, C.F. Pai, C.A. Ross, G.S.D. Beach, Spin transport in as-grown and annealed thulium iron garnet/platinum bilayers with perpendicular magnetic anisotropy, Phys. Rev. B 95 (11) (2017), https://doi.org/ 10.1103/PhysRevB.95.115428.
- [14] R.F. Pearson, Magnetocrystalline Anisotropy of Rare-Earth Iron Garnets, Proceedings of the Seventh Conference on Magnetism and Magnetic Materials, 1962, pp. 1236–1242, doi: 10.1007/978-1-4899-6391-8 87.
- [15] J.J. Bauer, E.R. Rosenberg, C.A. Ross, Perpendicular magnetic anisotropy and spin mixing conductance in polycrystalline europium iron garnet thin films, Appl. Phys. Lett. 114 (5) (2019), https://doi.org/10.1063/1.5074166.
- [16] E.R. Rosenberg, et al., Magnetic Properties and Growth-Induced Anisotropy in Yttrium Thulium Iron Garnet Thin Films, Adv. Electron. Mater. 7 (10) (2021) 2100452, https://doi.org/10.1002/aelm.202100452.
- [17] C.O. Avci, et al., Interface-driven chiral magnetism and current-driven domain walls in insulating magnetic garnets, Nat. Nanotechnol. 14 (6) (2019) 561–566, https://doi.org/10.1038/s41565-019-0421-2.
- [18] F. Büttner, et al., Thermal nucleation and high-resolution imaging of submicrometer magnetic bubbles in thin thulium iron garnet films with perpendicular anisotropy, Phys. Rev. Mater. 4 (1) (2020), https://doi.org/ 10.1103/PhysRevMaterials.4.011401.
- [19] A. Manchon, et al., Current-induced spin-orbit torques in ferromagnetic and antiferromagnetic systems, Rev. Mod. Phys. 91 (3) (2019), https://doi.org/ 10.1103/RevModPhys.91.035004.
- [20] Y. Fan, et al., Manipulation of Coupling and Magnon Transport in Magnetic Metal-Insulator Hybrid Structures, Phys. Rev. Appl. 13 (6) (2020), https://doi.org/ 10.1103/PhysRevApplied.13.061002.
- [21] X.Y. Sun, et al., Single-Step Deposition of Cerium-Substituted Yttrium Iron Garnet for Monolithic On-Chip Optical Isolation, ACS Photonics 2 (7) (2015) 856–863, https://doi.org/10.1021/acsphotonics.5b00026.
- [22] P. Dulal, et al., Optimized Magneto-optical Isolator Designs Inspired by Seedlayer-Free Terbium Iron Garnets with Opposite Chirality, ACS Photonics 3 (10) (2016) 1818–1825, https://doi.org/10.1021/acsphotonics.6b00313.
- [23] C.R. Warren, et al., Robust Perpendicular Magnetic Anisotropy in Off-Axis Sputtered Europium Iron Garnet (Euig) Thin Films, SSRN Electron. J. 560 (2022), https://doi.org/10.2139/ssrn.4043489.
- [24] N. Kumar, S. Prasad, D.S. Misra, N. Venkataramani, M. Bohra, R. Krishnan, The influence of substrate temperature and annealing on the properties of pulsed laserdeposited YIG films on fused quartz substrate, J. Magn. Magn. Mater. 320 (18) (2008) 2233–2236, https://doi.org/10.1016/j.jmmm.2008.04.112.
- [25] T. Goto, M.C. Onbaşlò, C.A. Ross, Magneto-optical properties of cerium substituted yttrium iron garnet films with reduced thermal budget for monolithic photonic integrated circuits, Opt. Express 20 (27) (2012) 28507–28527, https://doi.org/ 10.1364/op.20.028507
- [26] A. Heinrich, et al., Double-Layered Polycrystalline Iron Garnet Structure of Bi3Fe5O12 and Y3Fe5O12 grown on SiO2 substrates by pulsed laser deposition, J. Magn. Soc. Japan 32 (2_2) (2008) 130–134, https://doi.org/10.3379/ project 32.130
- [27] H.S. Kum, et al., Heterogeneous integration of single-crystalline complex-oxide membranes, Nature 578 (7793) (2020) 75–81, https://doi.org/10.1038/s41586-020-1320-r
- [28] M. Aldosary, et al., Platinum/yttrium iron garnet inverted structures for spin current transport, Appl. Phys. Lett. 108 (24) (2016), https://doi.org/10.1063/ 1.4953454
- [29] S. Strobel, C. Kirkendall, J.B. Chang, K.K. Berggren, Sub-10 nm structures on silicon by thermal dewetting of platinum, Nanotechnology 21 (50) (2010), https:// doi.org/10.1088/0957-4484/21/50/505301.
- [30] X. Tao, A. Eades, Alternatives to Image Quality (IQ) mapping in EBSD, Microsc. Microanal. 8 (S02) (2002) 692–693, https://doi.org/10.1017/ 1409786916455
- [31] W.M. Yim, R.J. Paff, Thermal expansion of AlN, sapphire, and silicon, J. Appl. Phys. 45 (3) (1974) 1456–1457, https://doi.org/10.1063/1.1663432.
- [32] Y. Okada, Y. Tokumaru, Precise determination of lattice parameter and thermal expansion coefficient of silicon between 300 and 1500 K, J. Appl. Phys. 56 (2) (1984) 314–320, https://doi.org/10.1063/1.333965.
- [33] S. Iida, Magnetostriction constants of rare earth iron garnets, J. Phys. Soc. Japan 22 (5) (1967) 1201–1209, https://doi.org/10.1143/JPSJ.22.1201.
- [34] A. Budkowski, et al., The compensation point in reig and some of its properties, J. Magn. Magn. Mater. 78 (2) (1989) 226–236, https://doi.org/10.1016/0304-8853(89)90272-2.

- [35] S. Geller, G.P. Espinosa, P.B. Crandall, Thermal expansion of yttrium and gadolinium iron, gallium and aluminum garnets, J. Appl. Crystallogr. 2 (2) (1969) 86-88, https://doi.org/10.1107/s0021889869006625.
 [36] B.D. Cullity, C.D. Graham, Introduction to Magnetic Materials, 2009.
- [37] S. Geller, J.P. Remeika, R.C. Sherwood, H.J. Williams, G.P. Espinosa, Magnetic study of the heavier rare-earth iron garnets, Phys. Rev. 137 (3A) (1965) A1034-A1038, https://doi.org/10.1103/PhysRev.137.A1034.
- [38] R. Pauthenet, Magnetic Properties of the Rare Earth Garnets, J. Appl. Phys. 30 (4) (1959) S290–S292, https://doi.org/10.1063/1.2185937.
 [39] G.F. Dionne, Molecular field coefficients of substituted yttrium iron garnets,
- J. Appl. Phys. 41 (12) (1970) 4874–4881, https://doi.org/10.1063/1.1658555.
 [40] A. Paoletti, Physics of Magnetic Garnets, North-Holland Pub. Co., Amsterdam, 1979.